Fuel Processing Technology 245 (2023) 107743

Contents lists available at ScienceDirect

Fuel Processing Technology

journal homepage: www.elsevier.com/locate/fuproc

Numerical simulation and mathematical models of ash deposition behavior considering particle properties and operating conditions

Xiang Liu [a,d], Xue Xue [a,c], Hui Li [a,b], Kelang Jin [a,c], Lei Zhang [a,d], Hao Zhou [a,c,*]

[a] Zhejiang University, Institute for Thermal Power Engineering, State Key Laboratory of Clean Energy Utilization, Hangzhou 310027, PR China
[b] China Huaneng Group CO., LTD, Beijing 100031, PR China
[c] Jiaxing Research Institute, Zhejiang University, PR China
[d] Zhejiang Key Laboratory of Clean Energy and Carbon Neutrality, PR China

ARTICLE INFO

Keywords:
Unified model
Thermophoresis
Adhesion model
PCA and BP
OpenFOAM

ABSTRACT

A unified model is proposed considering thermophoresis, erosion, dynamic mesh techniques and mixed particle adhesion model based OpenFOAM open-source software. The effects of particle concentration, particle size distribution, flow velocity, probe and air temperature were discussed. Results show that the unified model predicts the deposition thickness at the probe with an average error of 7.66%. Deposition and impact efficiency always show opposite trends to factor changes, which are dominated by particle temperature and size distribution, respectively. Impact efficiency is distributed in 50–65% and the deposition efficiency is 5–25%, which get the efficiency of forming deposition of any ash particles in the boiler may be 2.5–16.25%. Different factors affect the deposition efficiency by influencing the particle temperature, the average particle temperature rises by 30 K with a double increase in flow rate. Also, a change of 10 to 30 K in particle temperature corresponds to a change of 100 K in air temperature. Mathematical models of PCA and BP neural networks based on broad data were proposed, which predict the maximum deposition thickness and probe deposition morphology with an error of 15% and 8.9%. The results of this study can provide a monitoring method and reference for boiler operators and researchers.

More than half of the coal consumption is concentrated in coal-fired power station boilers and industrial boilers, while the quality of coal used for power is generally poor with high sulfur and ash content. Therefore, it is easy to form a series of problems such as ash accumulation, corrosion and wear on the heating surface of the boiler [1–3]. Among them, the problem of ash accumulation has been the biggest problem in coal-fired thermal power plants in terms of safe operation, which reduces the efficiency of the boiler and increases the operating costs of the plant. Therefore, it is necessary to strengthen the research on the mechanism of ash deposition, which is very important for reducing or inhibiting ash deposition in the heating surface [4–6]. Meanwhile, it is of great practical importance to ensure the safe operation of boilers, reduce the operating costs of power plants and protect the environment [7,8].

Ash deposition is a complex physico-chemical process involving several research points, such as multiphase flow, heat and mass transfer. Shimogori et al. [9]. evaluated the effect of microfine particles and alkali metal substances on the initial stages of ash deposition and the reduction in heat flow density. Naruse [10] et al. investigated the characteristics of ash generation from different pulverized coals under high-temperature conditions and found that ash deposition was related to the size of the ash particles produced, the flow field around the deposition probe and the composition of each ash particle. Liu [11] et al. performed an electron microscopic analysis of probe ash samples from high alkali coals and compared the ash deposition data from Li et al. [12]. Results indicated that the main mechanism of probe ash layer formation was thermophoretic and condensation deposition. At high Re numbers, the dominant ash deposition mechanism on the leeward side of the probe is inertial collision and thermophoretic deposition. With the rapid development of CFD technology, more and more scholars are using numerical simulation to solve the deposition process of particles and obtain good results. Simulation results from numerous authors have shown that there are five main ash deposition mechanisms [13–15]: inertial collision, thermophoretic deposition, condensation deposition, chemical reaction

* Corresponding author at: Zhejiang University, Institute for Thermal Power Engineering, State Key Laboratory of Clean Energy Utilization, Hangzhou 310027, PR China.

E-mail address: zhouhao@zju.edu.cn (H. Zhou).

https://doi.org/10.1016/j.fuproc.2023.107743
Received 3 January 2023; Received in revised form 5 March 2023; Accepted 13 March 2023
Available online 29 March 2023

and turbulent collision. Weber et al. [14]. concluded that inertial collision is the dominant mechanism in the fly ash deposition process, mainly reflected in the collision between larger fly ash particles (particle size >10 μm) and the heated surface due to their inertia inability to follow the flow line around the obstacle. The inertial collision efficiency of fly ash particles on the heated surface in crossflow can be expressed as a function of the Stokes number [16]. Yang et al. [17]. introduced a correction parameter Fi based on the collision rate formula at lower mesh numbers to obtain accurate collision rates for fine particles. Thermophoresis is the phenomenon of particle migration in the effect of temperature gradients and has been one of the main mechanisms of fine particle deposition by several scholars [18]. When there is a temperature gradient in the flow field to which the particles are subjected, the particles are affected by a thermophoretic force in the direction of the decreasing temperature gradient, with the main acting particles being <10 μm [19]. Models for determining the adhesion probability of particles with a probe are essential for the accuracy of numerical simulations of particle deposition. Researchers have developed three main particle adhesion models for determining the state of particles after impact. The three models: Empirical models based on viscosity [20–22], melt phase occupation [23,24] and critical velocity models [25,26]. Wielan [7] combined experimental data and simulation results to indicate that the three models yielded similar simulation results at low temperatures. In contrast, the empirical model based on viscosity and the molten phase occupation model was more accurate at high temperatures.

In summary, more and more new models are being proposed to improve the accuracy of ash deposition thickness prediction. However, no unified deposition prediction model considers multiple sub-models and dynamic mesh techniques. The static mesh does not consider the effect of ash deposition on the geometry of the calculation area, which caused the program to calculate the wrong particle impact location and gas-solid flow field distribution. The dynamic mesh technique used by Zhou [35] and Liang [39] et al. solves this problem very well. However, they did not consider the thermophoretic force of the ash particles and the new adhesion model by using 2 to 3 sub-models. In this paper, a highly unified model for predicting ash deposition behavior is developed based on OpenFOAM open-source computing software, taking into account dynamic mesh technology, particle residual energy adhesion theory, erosion and thermophoretic models. Based on this model, the effects of particle size, flow rate, particle concentration, probe temperature and air temperature on the microscopic and macroscopic properties of ash deposition at the pipe wall were investigated below. Finally, based on a large amount of simulation data, a mathematical model(the mathematical formula which can directly calculate the deposition thickness and morphology from several known variables) for predicting the thickness and morphology of ash particle deposition is established by data processing methods such as statistics and machine learning. To highlight the application scenarios of this work, two points are worth being pointed out. The first one is that the unified model established in this work is only used to study the deposition process of solid ash particles, the impact and flow behavior of liquid slag particles on the pipe wall are not considered. The second point is that machine learning has been introduced only to demonstrate that the technique can be used to predict the depositional morphology under multifactorial effects. Later scholars can appropriately use this technique to carry out prediction of depositional behavior of different types of particles. The unified calculation model established and the results discussed provide a strong theoretical guide to accurately predict the ash deposition thickness and propose control measures correspondingly.

1. Models and methods

1.1. Gas and solid phase control equations

The MPPIC (Muti-Phase Particles In Cell) method is an Eulerian-Lagrangian approach that solves for fluids as continuous and particles as discrete phases. Compared to the commonly used two-fluid model (TFM), the Euler-Lagrange method can accurately characterize the particles' migration trajectory and deposition behavior but it is computationally intensive. The MPPIC method uses numerical methods to achieve high computational efficiency and accuracy at the same time. The flow of the gas phase is described by a volume-averaged N-S control equation, while the motion of each particle is tracked for the solid phase. Representing a large number of particles with the same properties as numerical particles greatly reduces the number of particles to be tracked. Instead of dealing with collisions between particles directly, a particle stress model is used to prevent excessive buildup beyond the particle volume fraction limit, thus MPPIC method can indirectly avoid the appearance of physical unreality.

1.1.1. Gas phase control equations

Since the gas-solid flow studied in this paper does not involve chemical reactions and interphase mass transfer, the gas-phase behavior is described using continuity and momentum equations based on volume averaging as shown in Eq. 1 and 2 [27]. Where α is the continuous phase fraction (the gas phase), u is the gas phase velocity (i = 1,2, two-dimensional calculation domain in this work), u_{eff} is the effective kinetic viscosity and F_f is the momentum transfer term between the gas phase and the discrete phase.

$$\frac{\partial \alpha}{\partial t}+\nabla\cdot(\alpha u_i)=0 \tag{1}$$

$$\frac{\partial \alpha u_i}{\partial t}+\nabla\cdot\left(\alpha u_i u_j\right)=-\nabla p+\nabla\left(\mu_{eff}\nabla u\right)-F_f \tag{2}$$

1.1.2. Solid phase control equations

In the Euler-Lagrange method, the particle phase motion is obtained by solving the kinetic equations based on Newton's second law. In this paper, we combine the MPPIC method based on the Euler-Lagrange method to solve for the motion of the ash particles [28]. The MPPIC method includes a particle stress term, the continuity and momentum equations for the particles solved within the mesh to reduce the computational effort. A distribution function f(x, v; p_b, v_b, t) describes the parameters of particle motion, where x is the position of the particle, v is the velocity of the particle, p_b is the density of the particle, V_b is the volume of the particle and t is the time of particle motion. In this study, it is assumed that there is no mass exchange between particles,while density and diameter of all ash particles are uniform. Therefore, the distribution function is only a function f(x, v, t) of x,v,t, which can be obtained by solving the following Eq. 3 [29].

$$\frac{\partial f}{\partial t}+\nabla_x\cdot(fv)+\nabla_v\cdot(fA)=0 \tag{3}$$

Where ∇x is the scatter operator on spatial position, ∇_v is the scatter operator on velocity and A is the acceleration term, which includes the various forces acting on the ash particle. The specific expression for A is shown as Eq. 4, D is the drag coefficient in 1/s; ρ_s is the density of the particles in kg/m^3; τ_p is the stress between the particles in Pa; θ is the volume fraction of the particle phase within the mesh cell.

$$A=\frac{\mathrm{dv}}{\mathrm{d}t}=D(u-\mathrm{v})-\frac{1}{\rho_s}\nabla_x p+g-\frac{1}{\theta\rho_s}\nabla_x\tau_P \tag{4}$$

1.2. Thermophoretic force of particles

Several scholars [2,12,18,30] have confirmed that thermophoretic forces significantly influence the deposition of fine particles by experiments and CFD methods. Therefore, this work implants a thermophoretic force model applicable to ash particles in the OpenFOAM open-source calculation program as shown in Eq. 5 and 6.

$$\overrightarrow{F_{th}} = -\varphi \frac{d_p \mu_g^2}{2\rho_g T_g m_p} \nabla T \tag{5}$$

$$\varphi = \frac{12\pi C_s \left(k/k_p + C_t Kn\right)}{\left(1 + 3C_m Kn\right)\left(1 + 2k/k_p + 2C_t Kn\right)} \tag{6}$$

φ is the coefficient of thermophoresis, T_g is the gas temperature in K, m_p is the particle mass in Kg, u_g is the gas phase viscosity in Pa·s, d_p is the particle diameter in m; C_s is taken as 1.17, C_t as 2.18, C_m as 1.14, k and k_p are the fluid thermal conductivity and particle thermal conductivity in W/(m·K) respectively, and K_n is the Knudsen number.

1.3. Particle temperature model

During gas-solid flow, ash particles are subjected to both flame radiation and convective heating during transport, resulting in a rapid increase in particle temperature, which is important for determining the state of the ash particles after impacting with the probe. The molten phase occupation model proposed by Weber et al. [31,32] is based on particle temperature and probe surface temperature, so the present work considers radiation and convection heating into the particle energy equation in the form of a source term, as shown in Eq. 7.

$$m_p c_p \frac{dT_p}{dt} = hA_p\left(T_\infty - T_p\right) + \varepsilon_p A_p \sigma\left(\theta_R^4 - T_p^4\right) \tag{7}$$

Where c_p is the specific heat capacity of the particle in J/(kg·K); T_p is the temperature of the particle in K; A_p is the heated area of the particle in m^2; ε_p is the radiation emissivity of the particle respectively; θ_R is the radiation temperature in K. Based on the Reynolds number of the particle and the Prandtl number of the particle, assuming that the particle is spherical, we use the Ranz and Marshall [33] correlation to calculate the film heat transfer coefficient h.

1.4. Adhesion models coupled with molten phase occupancy and energy residual theory

The state of the ash particles after impact with the probe is an important factor affecting the deposition thickness. A model for calculating the probability of particle deposition based on the melt phase percentage has been used by many scholars around the world as shown in Eq. 8 [2,7]. Firstly, the method requires the software Factsage 5.2 to calculate the melt phase percentage of ash particles at different temperatures. Secondly, the trend between melt phase percentage and particle temperature is fitted. Finally, the melt phase percentage-temperature function is implanted into the particle deposition judgment sub-model to determine adhesion when the particles hit the probe. Where: η_{stick} is the probability of adhesion of particle p; $\eta_p(T_p)$ is the proportion of molten phase in the particle at a temperature of T_p; $\eta_s(T_s)$ is the proportion of molten phase in the deposit on the probe surface corresponding to the probe temperature T_s.

$$\eta stick = \eta_p\left(T_p\right) + \left(1 - \eta_p\left(T_p\right)\right)\eta_s(T_s) \tag{8}$$

However, fusion-free particles cannot be deposited if the model is only based on the molten phase percentage of particles, which is inconsistent with reality. Thus, particle energy residual theory was used to model the adhesion of fusion-free particles. The combination of these two models can describe the full range of particle adhesion behavior and the ash particle deposition process in detail. Yang [2,17] et al. analogized the deposition process of ash particles on probes to the diffusion and sticking behavior of droplets striking a wall. The deposition behavior of ash particles is described using the physical process of droplet impact on a wall. Therefore, the four-stage control equations for impact process were used and obtained an adhesion model based on particle energy residual theory as shown in Eq. 9 and 10. Where E* is the residual energy of the particle after impacting the probe, dm is the maximum spread ratio of the ash particles and θ is the contact angle between the particles and the probe. The determination rules for the new particle adhesion model developed in this work are as follows. (1) Firstly, the deposition probability of the particles impacting the wall was calculated based on the molten phase occupation model. It indicated that the probe deposition and the particles were molten on at least one side if the deposition probability was >0, then the particles were determined to be deposited based on this adhesion probability. (2) If the probability of deposition is equal to 0, indicating that neither the probe deposit nor the particle is fused, the adhesion state of the particle is determined according to the energy residual theory, then the particles were determined to be deposited based on this adhesion probability as shown in Eq. 10.

$$E^* = \frac{1}{4}d_m^2(1 - cos\theta) + \frac{2}{3d_m} - 0.00536{*}d_m^{4.70}{*}(1 - cos\theta)^{0.591} - 1 \tag{9}$$

$$\eta stick = exp\left[-9.21{*}E^*{*}\eta_p\left(T_p\right)\right], E^* > 0 \tag{10}$$

1.5. Erosion model

The phenomenon of rebound particles carrying away some of the deposited particles is called erosion. The additional mass of particles carried by the rebounding particles is related to the energy consumed after impacting the probe and the fusion percentage of the deposited surface. The energy required to carry deposited particles can be calculated as Eq. 11 [11,34], where d_{dep} denotes the average particle size of the deposited body and γ denotes the sodium sulfate surface energy.

$$\Delta E_{dep} = 2\gamma A_{dep} = 2\gamma\pi d_{dep}^2\left(1 - \sqrt[3]{1 - \eta_s}\right) \tag{11}$$

The erosion rate e is defined as the ratio of carry-away deposition to the mass of the impacting particles and is given in Eq. 12, where the correction factor ε is taken as 0.05 in this paper [35].

$$e = \varepsilon \frac{d_{dep}(E - E')}{2\pi\gamma d_p^3\left(1 - \sqrt[3]{1 - \eta_s}\right)} \tag{12}$$

1.6. Dynamic mesh method

There have been many studies based on numerical simulations to learn the ash deposition process of probes, but most of them have not considered the effect of deposition morphology on particle flight in real-time. It is well known that the deposition morphology changes the shape of the probe and thus has a significant effect on the flow field. The inertial impact is one of the main sources of ash particle deposition, so the effect of probe shape on the flow field must be considered exhaustively. This work introduces a non-stationary dynamic mesh approach to the MPPICFoam solver in calculating the effect of probe shape on particle migration in real time, where the probe shape changes and reconstructs the computational mesh under the deposition of large amounts of fly ash.

At the same time, the surface temperature of the ash deposition is constantly increasing as the deposition thickness increases in the probe. This change can significantly affect the adhesion state between the particles and the probe. Therefore, this work considers this property change and performs a real-time calculation of the probe temperature.

The fundamentals of the OpenFOAM dynamic mesh method need to be further explained, this method is inside the MPPICFoam solver and consists of the following parts. (1) Generate the corresponding mass matrix based on the mesh at the probe; (2) Record the mesh number where the ash particles impact and determine whether the particles are deposited, and if so, accumulate the mass values of the corresponding mesh numbers; (3) Average the three deposited masses before and after each mesh cell to ensure reasonable physical significance and numerical stability [35]; (4) Calculate the deposition thickness based on the mass matrix combined with the geometric information of the probe; (5)

Correct the geometric information of the probe based on the deposition thickness to achieve dynamic changes of the probe. A schematic diagram is shown in detail in Fig. 1 [31] below.

1.7. Calculation process

A schematic diagram of the particle deposition simulation process in the MPPICFoam solver is shown in Fig. 2. A non-stationary model was used to calculate the time-dependent particle deposition process. The specific simulation steps: (1) In one-time step, the MPPICFoam solver first solves the momentum, mass and energy equations for the gas and particle phases; (2) Based on sub-model 1, the particle temperature variation process is calculated based on the air temperature and particle flow field; (3) Combine the temperature field and sub-model 2 to obtain the thermophoretic force and correct the particle migration route; (4) The ash particles move along the calculated migration route and collide with the probes, determine the state of particle movement (bounce or deposition) according to sub-model 3; (5) Combine sub-models 3 and 4 to obtain the final mass of deposited particle in probe mesh cells and calculate the deposition thickness of each mesh; (6) The geometric information of the probes is corrected according to sub-model 5 in combination with the deposition thickness of each mesh, thus the entire calculation process in one time step is completed.

2. Simulation of working conditions

2.1. Geometric model and boundary conditions

As shown in Fig. 3, the length and width of the computational domain are 1200 mm and 350 mm respectively, with the high-temperature flue gas and ash particles flowing into the computational domain from left to right and the probe (40 mm outer diameter D and 38 mm inner diameter) placed across the center. This two-dimensional computational domain corresponds to the one-dimensional furnace chamber structure (350 mm diameter) from the experiments [36], where a structured grid was used to ensure numerical stability. In this work, the upper part of the mesh of Beckmann et al. [37] was established according to the theory of symmetric calculation to reduce computational resources and obtain better accuracy. Therefore, the whole furnace chamber was calculated symmetrically. In order to accurately calculate the heat and mass transfer near the probe, the mesh near the probe wall is encrypted, where the mesh size in the annular region is kept consistent at 0.5 mm. The results of the calculation domain meshing were shown in Fig. 3. The left side of the calculation domain is the inlet, where the flue gas and ash particles are released and set as the velocity inlet. The upper part of the calculation domain is defined as the wall with no slip and zero gradient boundary conditions for the velocity and pressure, respectively. The lower end of the calculation domain is defined as a symmetrical wall; the right end of the calculation domain is the outlet, which is set as a pressure outlet. Depending on the properties of the walls, the results of particle action on individual parts are not the same, as shown in Fig. 3.

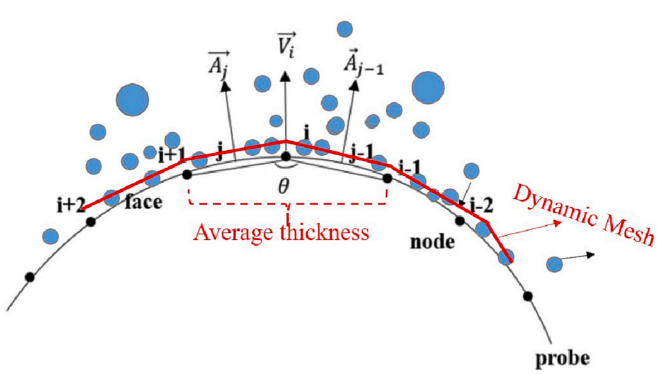

Fig. 1. Dynamic mesh technology within the MPPICFoam solver [31].

2.2. Simulation of working conditions parameter settings

In this study, the base parameters were derived from the work of Zhou [38] et al. Shanxi coal (SM) was used as the simulated medium, and its base information was in Table 1. The melt properties of SM within the literature [35] provide original data for the established particle adhesion model as shown in Fig. 4, and the function between percentage of the particle melt phase and temperature was in Table 1. It is worth pointing out that the program will default to 1 when the ratio of the molten phase of the particles is >1.

Currently, most studies have focused on the specific effects of five factors on ash particle deposition, wall temperature, air temperature, particle concentration, particle size distribution and flow rate. This work focuses on building a unified model for ash deposition thickness prediction considering the mutual coupling of five sub-models. Therefore, this paper discusses the effect of these five factors on ash deposition in detail based on the established unified model. The specific simulated working conditions are shown in Table 2. Cases 1–3 mainly discuss the effects of particle concentration on deposition and the basic properties of deposited particles; Cases 4–5, 6–7, 8–9, and 10–11 combined with Case 1 discuss the specific effects of particle size distribution, air temperature, wall temperature and flow rate on deposition thickness and deposition efficiency. Finally, the prediction models of deposition thickness and morphology are established separately based on the extensive simulation data.

In order to verify that the mesh size selected in this work has met the accuracy requirements, a mesh independence check was carried out according to the setup parameters of Case 1. The number of meshes is an important factor affecting the numerical simulation results. In this work, the ash deposition process was simulated with five different sets of meshes in order to eliminate the influence of the number of meshes on the deposition thickness results. When the number of meshes continues increasing but the deposition thickness no longer changes drastically, the amount of meshes is considered to have satisfied the calculation requirements. It can be seen from Fig. 5 that the difference between 64,000, 102,400 and 153,600 meshes is slight, and the numerical computation domain was divided into 64,000 meshes in this work to reduce the computational load and save computing time. However, it is worth pointing out an interesting phenomenon: the deposition thickness does not increase monotonically with the number of meshes. The authors assume that the complex process of ash particle deposition and dynamic meshes make it difficult for the deposition thickness to show a significant positive correlation with a particular factor.

3. Results and discussion

3.1. Validation of the model

This work carries out Case 1 based on the experiments of *Ma* [36] et al. which is used to verify the accuracy of the model as shown in Fig. 6. It is well known that the temperature and flow fields are the most important factors affecting particle deposition. The airflow velocity is significantly reduced in front of the probe, which is very beneficial for the deposition behavior of the ash particles. In contrast, the airflow velocity increases significantly in the region above the probe, which is consistent with the simulation results of Liang [39] et al. The large temperature gradient near the probe significantly affects particle deposition [40] based on the definition of thermophoretic forces [2,41]. Ash particles continuously hit the probe wall by inertia and thermophoretic forces, while the back of the probe is almost free of ash particles due to the airflow. The simulation results of the unified model are consistent with the simulation clouds of Zhou [35] et al. proving the accuracy of the modified MPPICFoam solver, and then the accuracy of

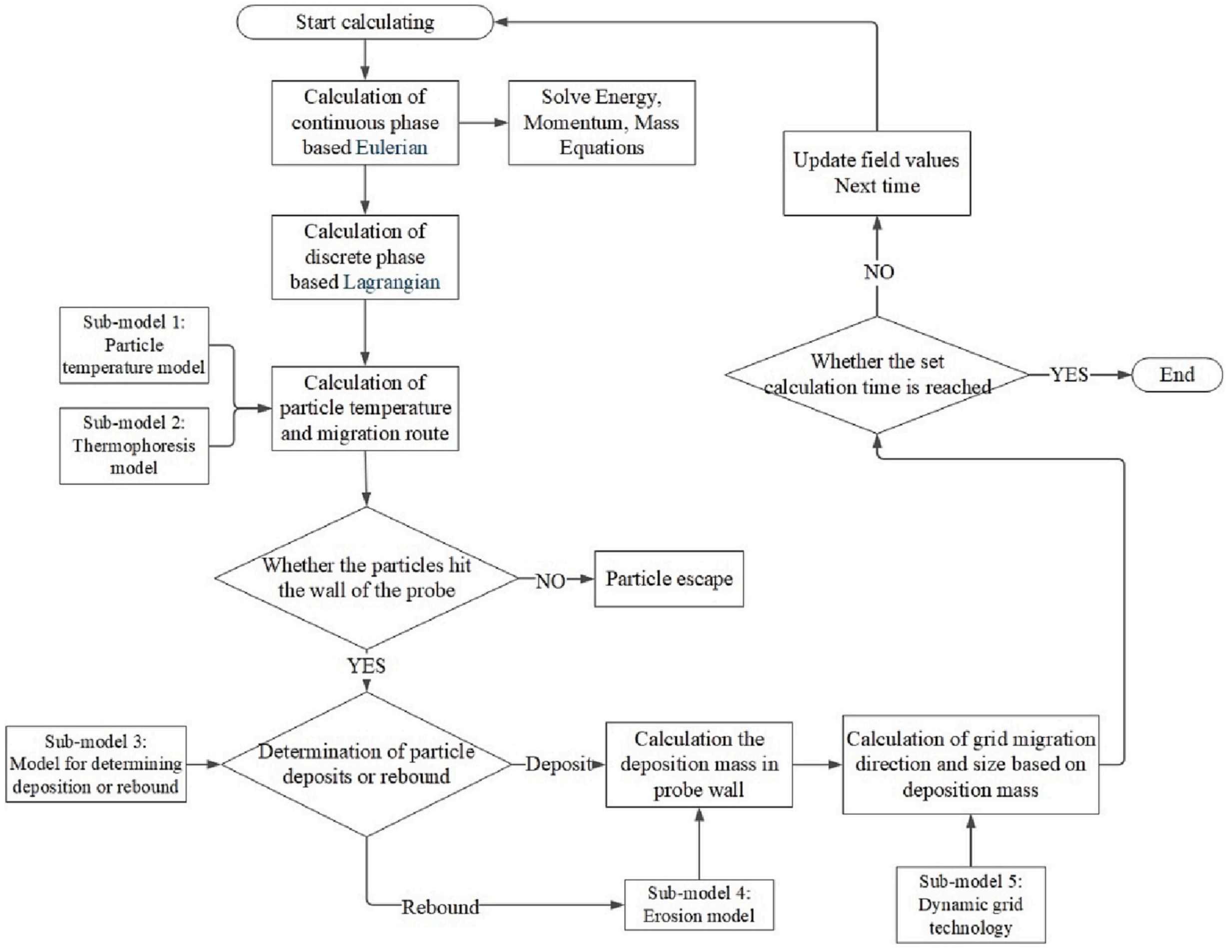

Fig. 2. Flow chart of the calculation of ash particle deposition for the coupled model. Fig. 2 cited to "A unified model of ash particle deposition behavior with thermophoresis and dynamic mesh based on OpenFOAM" under review manuscript number JFUE-D-23-00026.

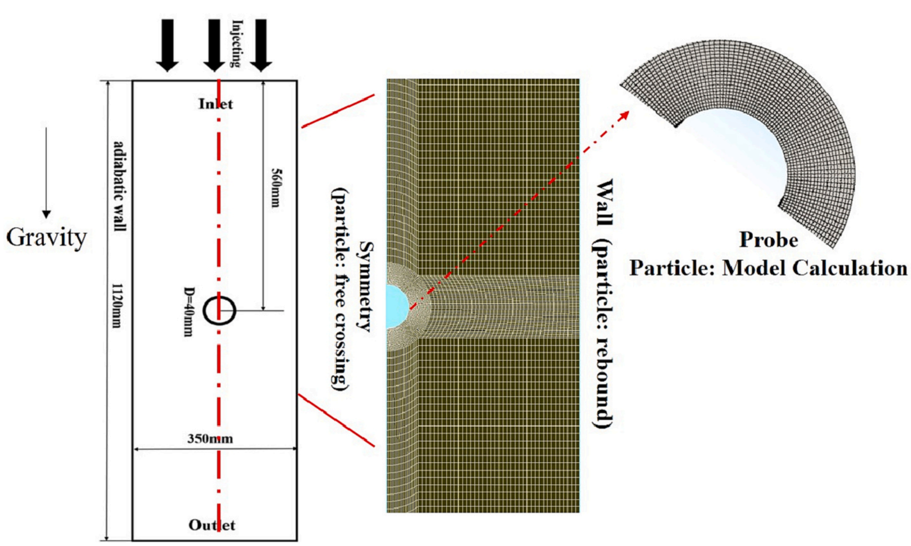

Fig. 3. Geometric model and boundary conditions.

the model is verified by quantitative comparison below.

A comparison of the experimental data and model calculations in probe deposition thickness is shown in Fig. 7.a. Improved MPPICFoam solver has a good prediction of the ash deposition process with an average error of 7.66% compared to the experimental value, confirming that the thermophoretic force model mentioned by Yang et al. [17] is very important in ash deposition. Based on the simulation results, the deposition surface temperature and heat flow density were calculated as shown in Fig. 7.b. The coupled model is reasonably accurate in predicting the deposition surface temperature and heat flow density, with

Table 1
Basic properties of ash particles.

Ash compositions		MPPIC parameters		Function	
Item	Value	Item	Value	Temperature (K)	Molten fraction(%)
Na_2O	0.74	Max. diameter (μm)	62	$T \leq 1083$	0
MgO	1.08			$1083 < T \leq 1123$	
Al_2O_3	20.22	Min. diameter (μm)	1	$15–2.2 \times 10^{63}\exp(-T/7.56)$	
SiO_2	48.58			$1123 < T \leq 1353$	
P_2O_5	0.25	Avg. diameter (μm)	28.5	$15.8 + 3.06 \times 10^{-13}\exp(T/42.58)$	
K_2O	1.26			$1353 < T \leq 1463$	
CaO	21.23	Thermal conductivity (W/m/K)	0.5	$31.3 + 1.52 \times 10^{-9}\exp(T/61.49)$	
TiO_2	0.73			$1463 < T \leq 1663$ $44.9 + 0.0053\exp(T/179.92)$	
MnO_2	0.25	Density (kg/m3)	2500	T>1663	58.2 + 0.024 T

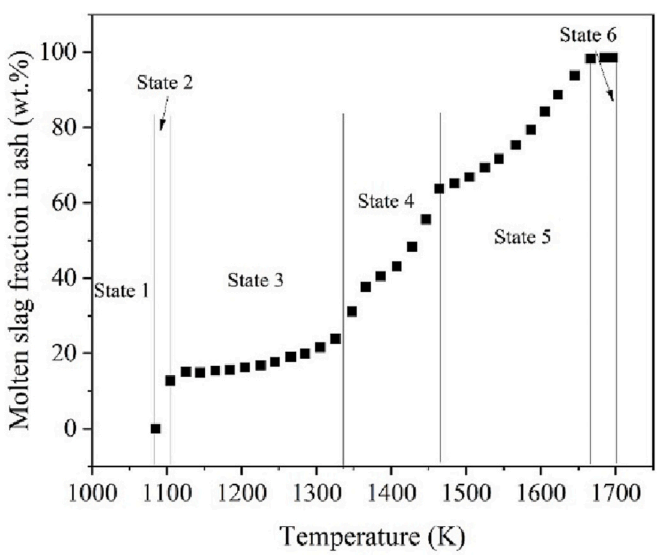

Fig. 4. Melting properties of SM at different temperatures [35].

Table 2
Simulation of working conditions.

Case	Particle concentration Kg/m/s(g/m^2)	Average particle size μm	Fuel temperature K	Probe temperature K	Inlet velocity m/s
1	0.0047(0.84)	28.5	1523	503	5.6
2	0.0094(1.68)	28.5	1523	503	5.6
3	0.00235(0.42)	28.5	1523	503	5.6
4	0.0047(0.84)	38.5	1523	503	5.6
5	0.0047(0.84)	48.5	1523	503	5.6
6	0.0047(0.84)	28.5	1423	503	5.6
7	0.0047(0.84)	28.5	1623	503	5.6
8	0.0047(0.84)	28.5	1523	406	5.6
9	0.0047(0.84)	28.5	1523	600	5.6
10	0.0047(0.84)	28.5	1523	503	2.8
11	0.0047(0.84)	28.5	1523	503	11.2

relative errors of 6.1% and 5.4%, respectively, compared to the experimental data of *Ma* [36] et al. As the deposition thickness increased, the deposition surface temperature increased rapidly and stabilized to 1250 K. The relative heat flow density decreased rapidly and then stabilized to 0.4, indicating that the deposition at the probe significantly worsened the heat transfer process. Also, simulation results from the literature [26,35] were used for comparison, and it can be seen that the unified model is more accurate in predicting some essential physical quantities of the ash deposition process. In addition, a comparison of the ash deposition morphology photographed by Zhou [38] et al. and the simulated morphology is shown in Fig. 8. It is worth pointing out that the numerical simulation using a dynamic mesh can describe the actual ash deposition process perfectly. The actual ash deposition morphology is depicted clearly, not only that the erosion at the front of the probe is also captured accurately, as shown in Fig. 8.

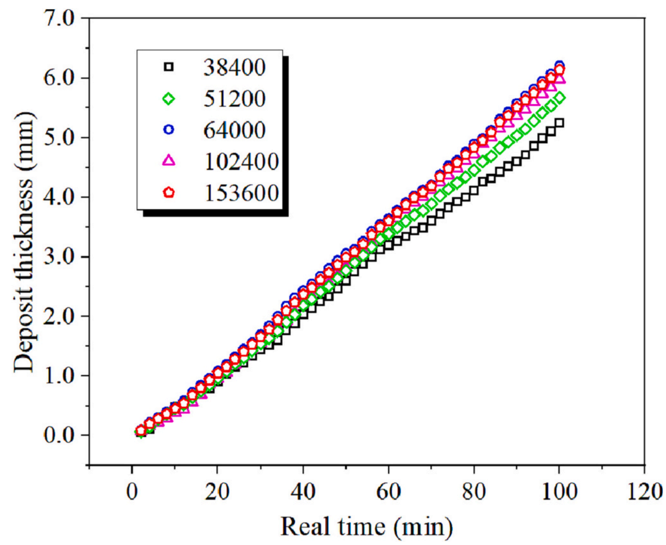

Fig. 5. Tests for mesh independence.

In summary, the three aspects of cloud distribution, deposition thickness data and morphological comparison confirm the excellent accuracy of the established coupled model. The specific influence of each factor on probe deposition will be discussed in the following section based on the coupled model.

3.2. *Effect of particle properties on deposition*

3.2.1. *Particle concentration*

Particle concentration is an important factor influencing wall deposition and has been studied by several authors [4,6,35]. The specific effect of particle concentration on wall deposition is investigated by comparing Cases 1, 2 and 3 (corresponding to fly ash yields of 0.0047Kg/m/s(0.84), 0.0094Kg/m/s(1.68) and 0.00235Kg/m/s(0.42) kg/h(g/m^2), respectively). As shown in Fig. 9.a, the deposition thickness and rate show an increasing trend with time. The authors believe there are two main reasons for this phenomenon. First, ash deposition changes the shape of the probe and ash particles are less likely to be deposited on circular probe walls. Second, the wall temperature increases and a molten state occurs as the thickness of the deposition increases, increasing the ability to capture particles. The deposition thickness tends to increase approximately linearly with increasing particle concentration in the range of 0.00235 to 0.0094 Kg/m/s as shown in Fig. 9.b, which has significant meaning for practical production. It can be seen from Fig. 9.c that the impact efficiency decreases with increasing particle concentration, but the deposition efficiency increases with increasing particle concentration and stabilizes with time. With particle concentrations of 0.00235 to 0.0094 Kg/m/s corresponding to impact efficiencies of 57 to 50% and deposition efficiencies of 14 to 16%. As can be seen from the properties of the deposited particles in Fig. 10.a, the deposited particle size increases slightly with increasing particle concentration, indicating that the particle concentration does not affect the selectivity of the probe for deposited particles. The particle deposition

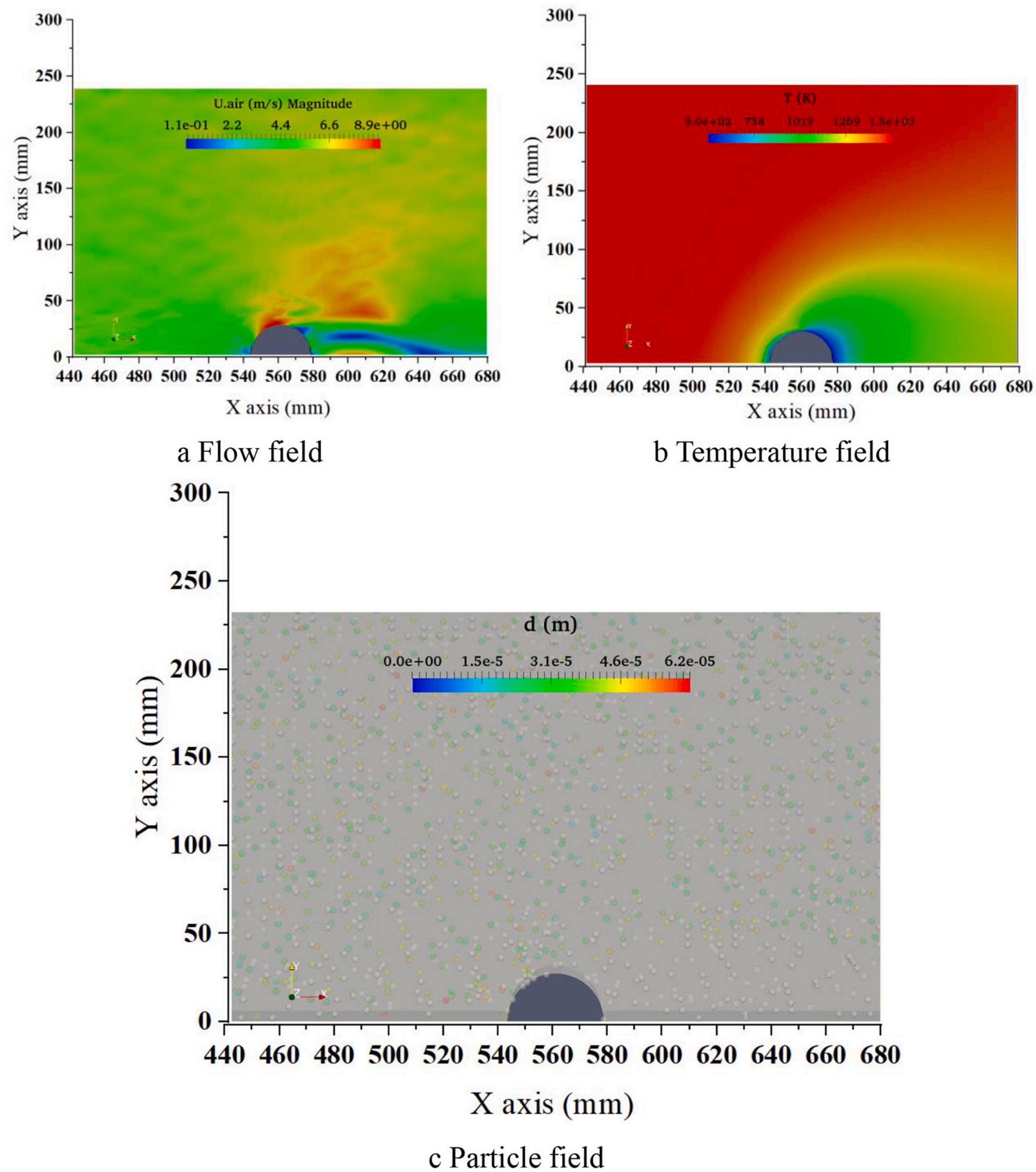

Fig. 6. Cloud distribution of flow, temperature and particle fields for Case 1.

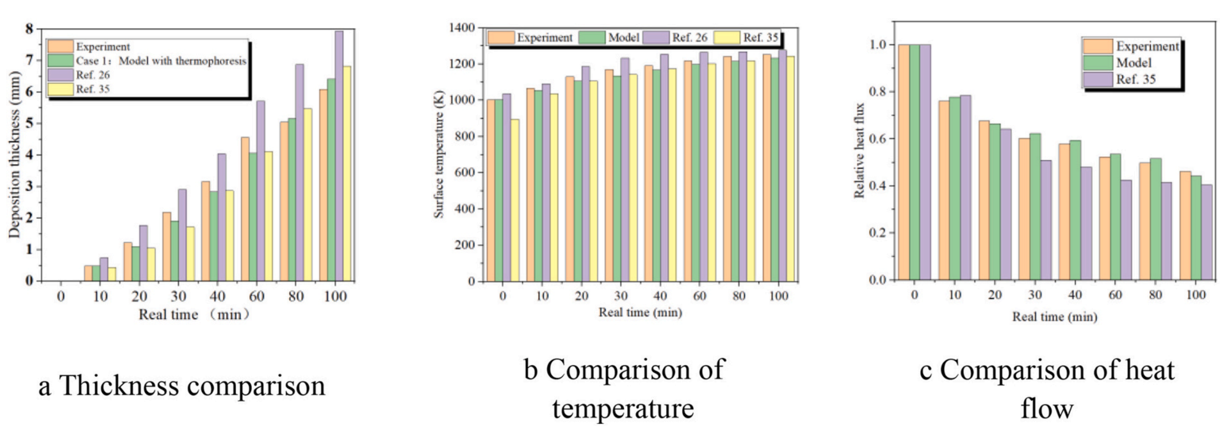

Fig. 7. Comparison of simulation results with experimental results.

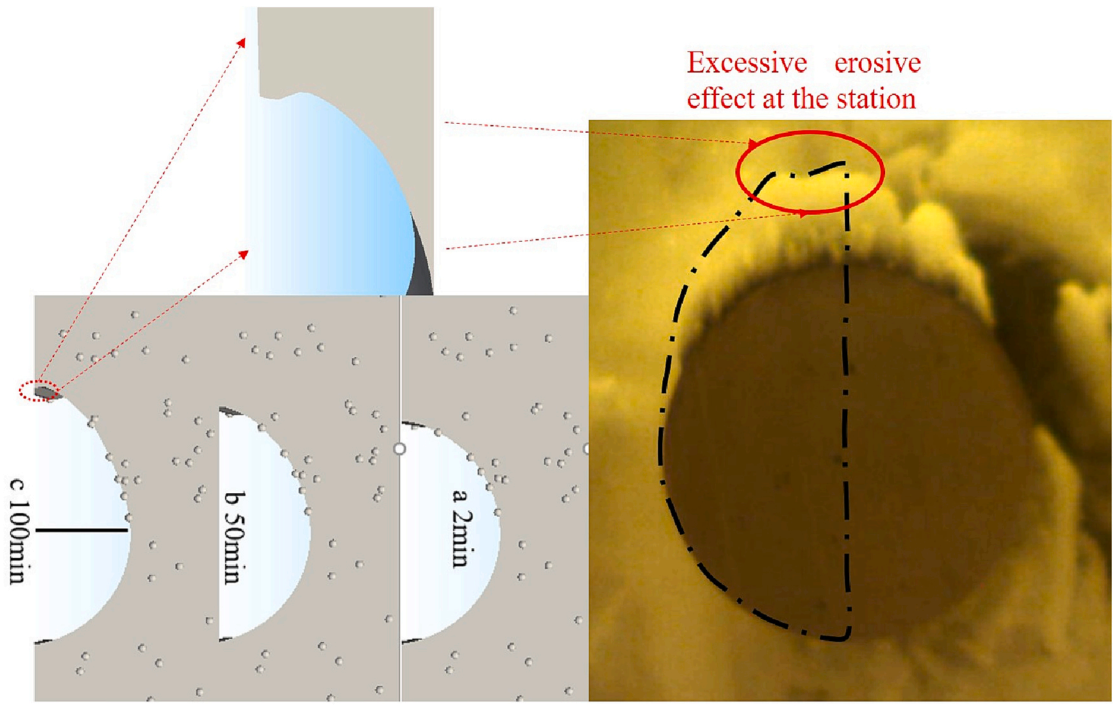

a Simulation results b Experimental results

Fig. 8. Comparison of simulated and experimental morphology.

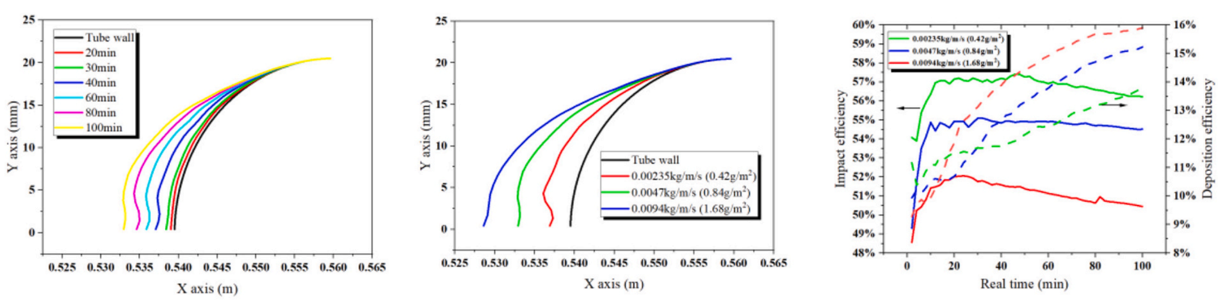

a Time b Concentration c Efficiency

Fig. 9. Trends in deposition over time and particle concentration.

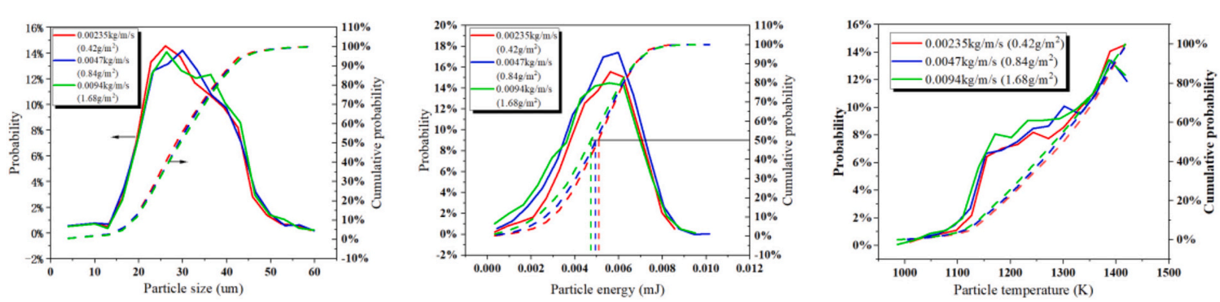

a Particle size b Particle energy c Particle temperature

Fig. 10. Analysis of deposited particle properties with different flow velocity.

energy shows a slight tendency to decrease as shown in Fig. 10.b, with a slight decrease in flow rate due to excessive particle loading. Higher concentrations lead to lower particle temperatures from Fig. 10.c which are consistent with particle energy. The authors concluded that the concentration could not significantly affect the particle properties in the furnace chamber because the actual ash content remains very low relative to the chamber volume. However, the number of particles captured by the probe increases significantly due to the increase in the number of particles leading to an increase in the deposition thickness.

3.2.2. Flow velocity

Liang [39] et al. studied the law of particle deposition at different flow rates and found that the difference in flow rate at different particle sizes (10, 30, 50 μm) led to different deposition behavior. For 10 μm particles, the deposition thickness increased as the flow rate increased; for 50 μm particles, the deposition thickness decreased as the flow rate increased; and for 30 μm particles, the deposition thickness first increased and then decreased. In this work, the deposition behavior of particles at three flow rates of 2.8, 5.6 and 11.2 m/s was investigated in Fig. 11.a and found that the deposition thickness increased with decreasing flow rate and stabilized at 6–7 mm in the later stages, which is different from the results of Liang et al. [39] The authors concluded that the results differed because the present work used a double R model to characterize the actual ash particle size distribution. In contrast, Liang et al. [39] used a homogeneous particle size (10, 30, 50 μm) to carry out simulations. In addition, two different particle deposition models were chosen to deal with the behavior of ash particles after impact with the probe, which led to inconsistent results. Liang [39] used a critical viscosity model and the present work uses a modified model, which combined melt volume fraction and energy residual theory to determine whether particles have been deposited. For the model implanted in this work, the flow rate increases as the melting state of the ash particles decrease, leading to a decrease in particle deposition efficiency. Therefore, further analysis of the trend in particle impact and deposition efficiency with flow rate as shown in Fig. 11.b, revealed that the impact efficiency increases with increasing flow rate and tends to stabilize at 54%. The deposition efficiency tends to decrease linearly with increasing flow rate and does not stabilize, indicating that the deposition efficiency may continue to decrease linearly with increasing flow rate, which is consistent with the study of Liang et al. [39]. In summary, the impact efficiency ranged from 51% to 54% and the deposition efficiency from 20% to 11% within the flow rate of 2.8–11.2 m/s; the deposition efficiency showed an increasing linear trend with time and leveled off in the later stages. Flow rate does not affect impact efficiency but significantly affects deposition efficiency.

As can be seen from the properties of the deposited particles in Fig. 12, the probability distribution of the deposited particles energy does not change with the flow velocity. Combined with the flow field data in Fig. 6.a, the velocity of the particles is already converging near the wall when they are trapped near the wall under the effect of the near-wall disturbance. The average particle size of the deposited particles gradually decreases as the flow velocity increases, with 2.8 m/s and 5.6 m/s corresponding to an average particle size of 30 μm and 11.2 m/s corresponding to an average particle size of 27 μm. The main reason behind this phenomenon is that lower temperature and less liquid phase of large particles at high flow rates result in lower deposition efficiency. In addition, the high flow rate has a significant selectivity for deposited particles, with about 80% of the deposited particles concentrated in the 20–40 μm range, a significantly higher proportion than the other working conditions of about 60%. The temperature distribution of the particles showed a significant difference, which is the reason for the difference in deposition efficiency. It can be seen from Fig. 12.c that the average particle temperature rises by 30 °C with a double increase in flow rate. Particle temperature significantly affects the percentage of molten phase of the particles and acts on the particle deposition efficiency.

3.2.3. Particle size

In this work, a double R model was used to simulate the real particle size distribution. The average particle size is an important parameter in the model, and an increasing average particle size indicates an overall shift of the particles towards larger particle sizes. By comparing the effect of three different mean particle sizes on the deposition thickness as shown in Fig. 13.a, we find that the deposition thickness decreases with increasing particle size. The deposition thickness does not change linearly with increasing mean particle size in the later stages. Also, the growth rate decreases significantly, indicating that there may be an average particle size threshold and the deposition thickness will not change if the particle size continues to increase. There are two main reasons for this phenomenon in conjunction with the results of Liang et al. [39], the higher fusion ratio of smaller particles leads to higher deposition efficiency, while smaller particles correspond to lower kinetic energy and particles are less likely to escape.

As shown in Fig. 13.b, further analysis of the particle impact efficiency and deposition efficiency shows that the impact efficiency increases with increasing ash particle size, but the increase rate gradually decreases. The deposition efficiency decreases with increasing particle size, and the rate of decrease also gradually decreases, indicating that with the increase of the average particle size, both efficiencies eventually stabilize at 65% and 7%. The average particle size of 28.5–48.5 μm corresponds to an impact efficiency of 50–67% and a deposition efficiency of 8.5–13%. Analysis of the two efficiency trends over time shows that the impact efficiency rises rapidly in the early stages and stabilizes after the first 40 min of deposition. In contrast, the deposition efficiency increases linearly and plateaus in the later stages with both efficiencies being a constant value in the later stages of deposition.

A deeper analysis of the deposited particle properties as shown in Fig. 14, shows that the average particle size of the deposited particles continues to increase with increasing input particle size, corresponding to 29 μm, 32 μm and 44 μm, respectively, and the average energy also

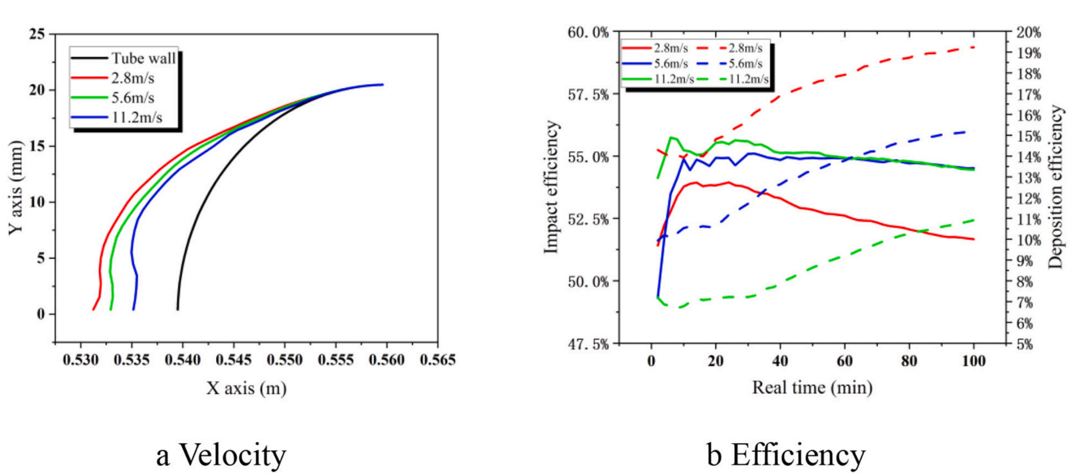

Fig. 11. Trends in deposition over time and flow velocity.

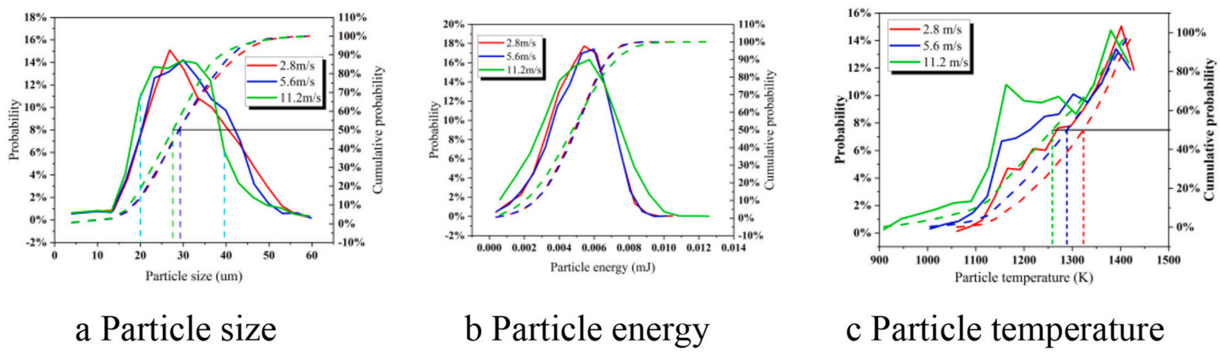

Fig. 12. Analysis of deposited particle properties with different flow velocity.

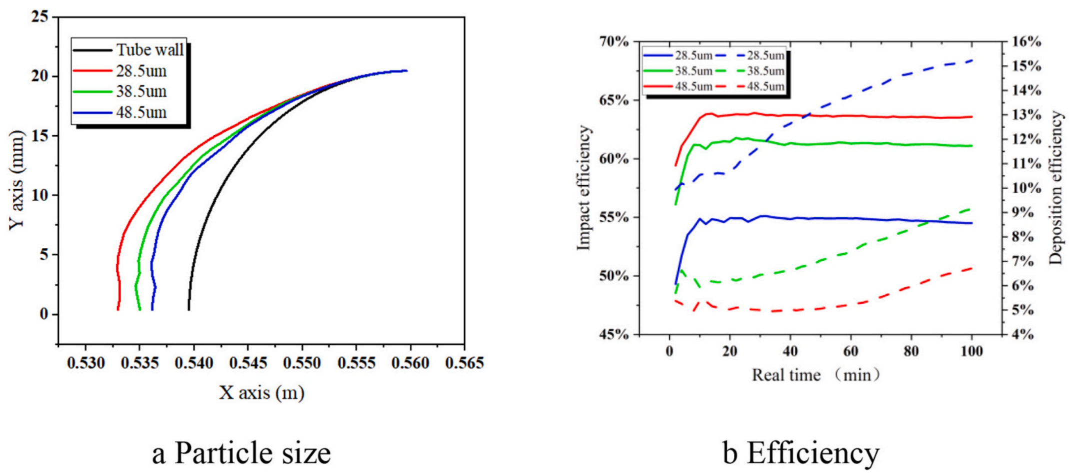

Fig. 13. Trends in deposition over time and particle size.

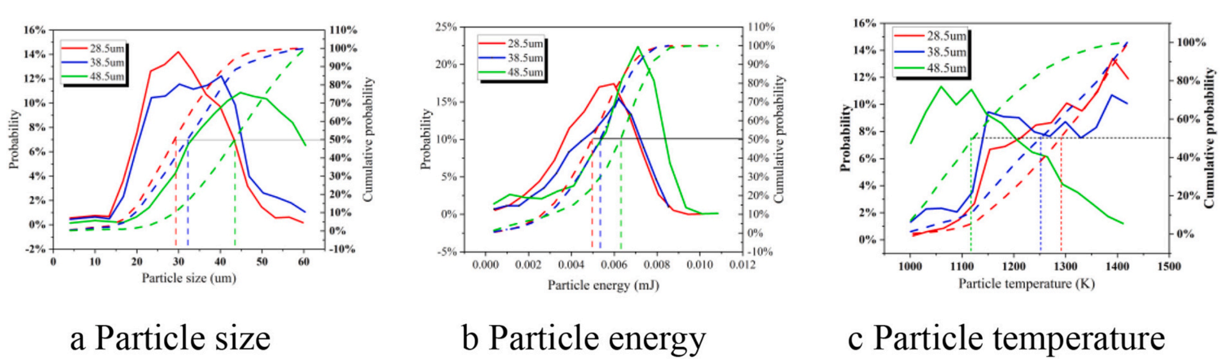

Fig. 14. Analysis of deposited particle properties with different particle sizes.

continues to increase, around 0.005 to 0.006 mJ. The temperature distribution probability curve for the deposited particles shows that the particle temperature decreases as the particle size increases, with an average temperature of 1125 K for 48.5 μm particles and 1300 K for 28.5 μm particles. The authors concluded that the larger specific surface area of small particles leads to higher heat obtained resulting in higher particle temperatures. As the temperature increases, the volume fraction of the liquid phase within the particles increases, leading to an increase in the deposition probability of smaller particles, as shown in Fig. 13.b.

3.2.4. Probe temperature

Probe temperature also affects the deposition of ash particles. This work investigated the effect of three probe temperatures on particle deposition behavior at 406 K, 503 K and 600 K. The deposition thickness increases with increasing probe temperature as shown in Fig. 15.a, but the change is insignificant and stabilizes at 600 K. The 406–600 K probe temperature corresponds to a deposition thickness of approximately 6 mm, and the simulation results are consistent with the results of Liang [39] et al. Although the difference in thermophoretic forces caused by varying the probe temperature slightly affected the deposition thickness, the particle impact and deposition efficiency varied with probe temperature as a result of thermophoretic forces in Fig. 15.b. As the probe temperature decreases, the impact efficiency decreases, but the difference is not significant and is concentrated around 55%. The deposition efficiency increases significantly with increasing probe temperature and stabilizes at 16%. The lower probe temperature creates a stronger thermophoretic force, increasing particle impact efficiency. At the same time, a higher probe temperature corresponds to a higher deposit

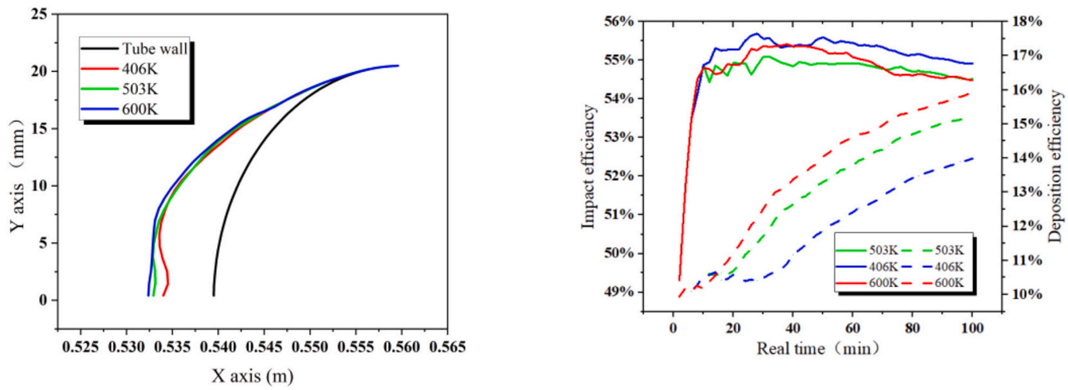

a Probe temperature b Efficiency

Fig. 15. Trends in deposition over time and probe temperature.

temperature, leading to a higher deposition efficiency. In addition, the deposition efficiency tends to increase linearly with time and then level off.

There is no significant change in the energy and size distribution of the deposited particles with probe temperature and probe temperature is not significantly selective for deposited particle properties as shown in Fig. 16. The authors supposed that the probe temperature affects the deposition efficiency of the particles mainly by changing the deposition surface temperature, which influences the deposition probability of the particles. Therefore, a conclusion was obtained that the probe temperature ranged from 403 to 600 K corresponding to a deposition efficiency of 14–16% and an impact efficiency of 55%.

3.2.5. *Air temperature*

For the effect of flue gas temperature, it can be found from Fig. 17 that the deposition thickness increases rapidly as the flue gas temperature increases from 1423 K to 1623 K and the deposition rate shows a growing trend, corresponding to 5, 6, and 10 mm. The impact efficiency decreases with increasing air temperature, but the change is not obvious and stable at 55%. Meanwhile, the deposition efficiency increases with increasing air temperature and shows an exponential trend corresponding to 10%, 16% and 24%, which is consistent with the increasing trend in deposition thickness. The deposition efficiency showed a linear trend with time, and the higher the air temperature is, the greater the slope of the linear increase, indicating that the deposition efficiency of the particles is influenced by both air temperature and time. There are two main reasons for the significant effect of air temperature on deposition thickness and deposition efficiency. First, the air temperature significantly affects the particle temperature in the form of radiation and convection, increasing the fusion ratio of the particles and improving the particle deposition efficiency. Second, the air temperature continuously heats the deposit, resulting in a higher melt ratio on the deposit surface and making it easier to capture particles. As shown in Fig. 18, the energy and particle size of the deposited particles increases with increasing air temperature, but the change is not significant. The average temperature of the deposited particles increases with increasing air temperature and the trend becomes larger, with a change of 100 K in air temperature corresponding to a change of 10 to 30 K in particle temperature.

In summary, there are differences in the effects and mechanisms of the five factors on particle deposition behavior, mainly in terms of particle impact and deposition efficiency. Concentration, particle size distribution and flow rate affect both impact and deposition efficiency, and probe and air temperature only affect deposition efficiency. Further analysis of the data shows that changes in mean particle size significantly affect the impact efficiency and that changes in flow rate, particle size and air temperature significantly affect the deposition efficiency. Combining the probability curves of the particle temperature distribution corresponding to the changes in flow rate, mean particle size and air temperature show that the particle temperature is the critical factor affecting the deposition efficiency. Therefore, Deposition and impact efficiencies are dominated by particle temperature and size distribution, respectively. From Table 3 below, the impact efficiency (Eff1) of particles under different working conditions is distributed in the range of 50–65%, and the deposition efficiency(Eff2) is distributed in the range of 5–25%, so we can get the efficiency of forming deposition of any ash particles in the boiler must be in the range of 2.5–16.25%. Once the mass flow rate of ash particles in the boiler is known, the thickness of the probe deposits in the actual operating boiler can be approximated. However, the above study is only a qualitative calculation of the deposition of the probes, and the data will be further processed and mathematically modeled to quantify the deposition thickness of the probes.

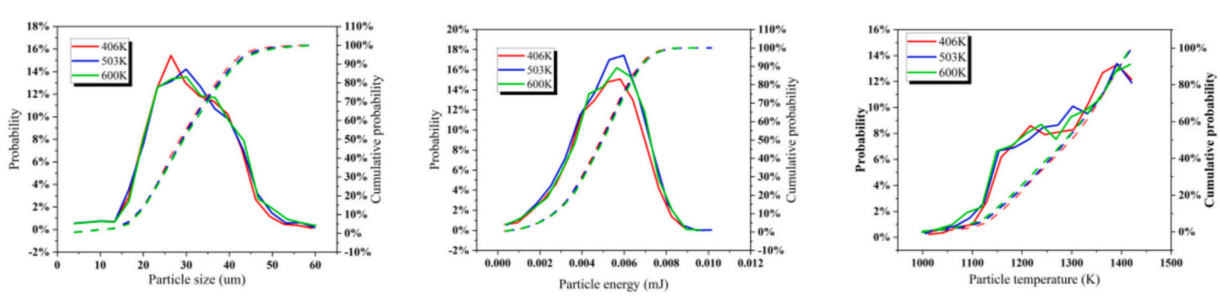

a Particle size b Particle energy c Particle temperature

Fig. 16. Analysis of deposited particle properties with different probe temperatures.

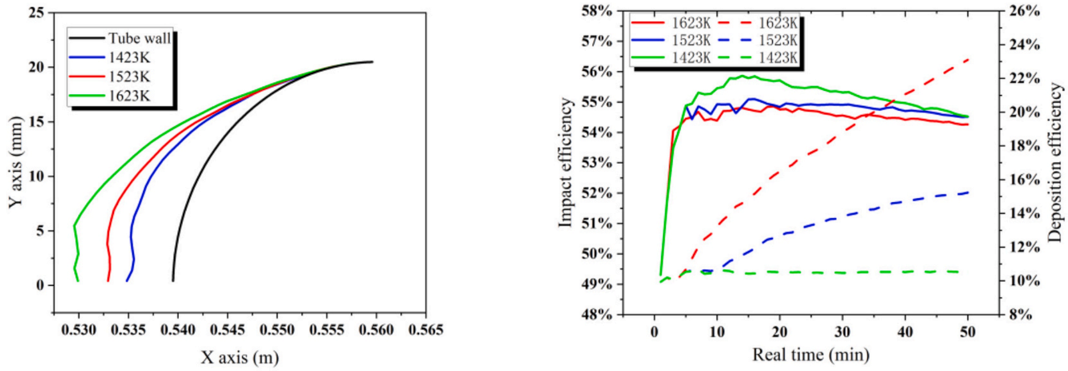

a Air temperature b Efficiency

Fig. 17. Trends in deposition over time and air temperature.

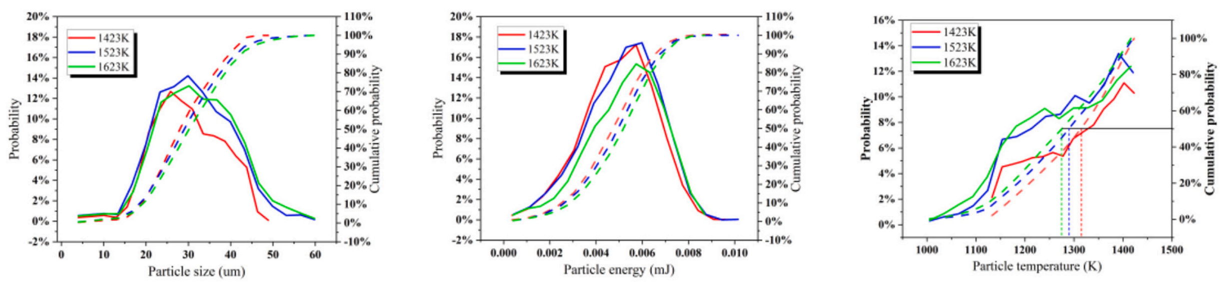

a Particle size b Particle energy c Particle temperature

Fig. 18. Analysis of deposited particle properties with different air temperatures.

Table 3
Impact and deposition efficiency of particles under different factors.

Factor	Concentration $\times 10^{-3}$/kg/s (g/m^2)			Flow velocity m/s			Particle size µm			Probe temperature K			Air temperature K		
Case	2.35 (0.42)	4.7 (0.84)	9.4 (1.68)	2.8	5.6	11.2	28.5	38.5	48.5	1423	1523	1623	406	500	603
Eff1	51%	55%	56%	51%	55%	55%	55%	61%	63%	55%	54%	54%	55%	54%	54%
Eff2	14%	15%	16%	11%	15%	19%	7%	9%	16%	10%	16%	24%	14%	15%	16%

3.3. Deposition thickness prediction model based on PCA

The trend in probe deposition thickness over time under different operating conditions is influenced by numerous factors. Independent analysis of all variables only leads to isolated conclusions and fails to take full advantage of all the information in the original data. Therefore, multiple variables that are closely related can be transformed into fewer new variables, thus representing all the information in the original data using fewer composite metrics. PCA (Principal Component Analysis) is an effective method for dimensionality reduction analysis of a large amount of original data. Firstly, the N-dimensional variables of the original data are mapped to K dimensions, which were known as principal components. Secondly, the eigenvalues and eigenvectors are obtained by calculating the covariance matrix of the data matrix by Eq. 13. Finally, the eigenvector matrix corresponding to the K features of the largest eigenvalue was used to realize the dimensionality reduction of a large amount of data. Where x_i is the independent variable, y_i is the dependent variable and n is the number of original data sets collected.

$$cov(X,Y) = E[(X-E(X))(Y-E(Y))] = \frac{1}{n-1}\sum_{n}^{i=1}(x_i-\overline{x})(y_i-\overline{y}) \tag{13}$$

The data were processed deeply using principal component analysis for multiple factors as shown in Table 4. It is worth pointing out that the first five of the six factors in Table 4 represent the five factors discussed earlier. In order for the field engineer to understand the operating conditions of the boiler at different times, this work introduces deposition time as the sixth factor and builds the model. The mathematical models for the six variables of probe deposition thickness and mean particle size, particle concentration, air temperature, wall temperature, flow rate and deposition time were obtained in Eq. 14. Where d is the mean particle size in µm; *Con* is the particle concentration in kg/m/s; *Tair* is the air temperature in K; *Twall* is the probe temperature in K; *Vec* is the particle flow rate in m/s; *Time* is the deposition time in min; *Thickness* is the probe deposition thickness in mm, note that the deposition thickness directly in front of the probe is chosen. Fig. 19 shows the high accuracy of the model predictions with an average error of only

Table 4
Analysis data for PCA.

$$Thickness = -0.02519 - 0.000133*d + 0.655252^{*}Con + 0.000017^{*}Tair + 0.000003^{*}Twall - 0.000269^{*}Vec + 0.0000745^{*}Time \quad (14)$$

Case	Average Particle size um	Concentration kg/m/s	Air Tem K	Probe Tem K	Velocity m/s	Time min	Thickness mm
Case1	28.5	0.0047	1523	503	5.6	50	3.324
Case1	28.5	0.0047	1523	503	5.6	100	7.266
Case2	28.5	0.00235	1523	503	5.6	50	1.796
Case2	28.5	0.00235	1523	503	5.6	100	3.788
Case3	38.5	0.0047	1523	503	5.6	50	1.852
Case3	38.5	0.0047	1523	503	5.6	100	5.044
Case4	48.5	0.0047	1523	503	5.6	50	1.369
Case4	48.5	0.0047	1523	503	5.6	100	3.848
Case5	28.5	0.0047	1523	406	5.6	50	2.787
Case5	28.5	0.0047	1523	406	5.6	100	6.577
Case6	28.5	0.0047	1523	600	5.6	50	3.312
Case6	28.5	0.0047	1523	600	5.6	100	7.289
Case7	28.5	0.0047	1523	503	2.8	50	4.205
Case7	28.5	0.0047	1523	503	2.8	100	8.268
Case8	28.5	0.0047	1523	503	11.2	50	2.237
Case8	28.5	0.0047	1523	503	11.2	100	5.344
Case9	28.5	0.0047	1423	503	5.6	50	2.522
Case9	28.5	0.0047	1423	503	5.6	100	4.762
Case10	28.5	0.0047	1623	503	5.6	50	4.267
Case10	28.5	0.0047	1623	503	5.6	100	10.441
Case11	28.5	0.0094	1623	503	5.6	50	6.479
Case11	28.5	0.0094	1623	503	5.6	100	12.441

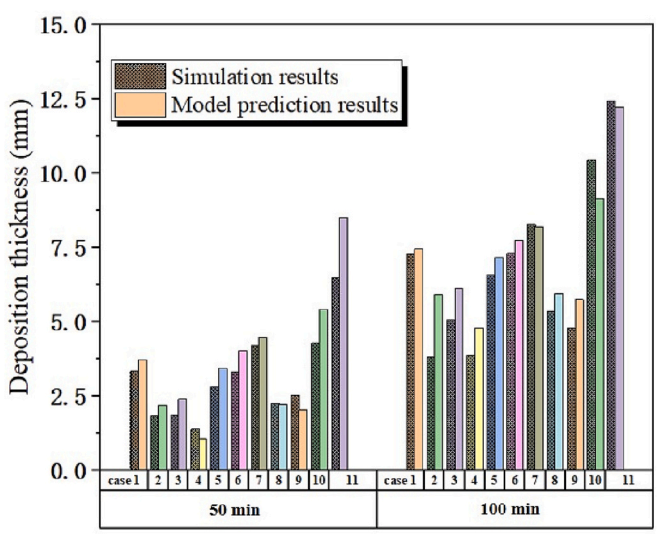

Fig. 19. Comparison of PCA prediction results.

15% when predicting the maximum deposition thickness over a longer deposition time.

3.4. Probe deposition models for machine learning

The deposition thickness model obtained based on PCA only predicts a certain position of the probe and cannot solve for the complete deposition profile. A total of 22,000 sets of data were obtained for deposition thicknesses from 0 to 100 min, 0 to 90°, and different operating parameters based on Case 1–11. In order to completely predict the deposition profile of the probes, this work uses machine learning to obtain a mathematical model to calculate the full range of probe deposition thicknesses. Back-propagation (BP) networks were first proposed by Rumelhart and McClelland [42] in 1986. BP uses the fastest descent method to learn and store the mapping relationships between a large number of variables, which adjusts the weighting factor of the variables continuously by back-propagation to minimize the sum of squared errors between the model and the actual values. The topology of the BP neural network model consists of an input layer, a hidden layer and an output layer. The topology of the BP neural network in this work is shown in Fig. 20. It is worth pointing out that the BP method proposed in this work is an attempt to predict the ash deposition morphology. The complexity of the ash particle deposition process leads to no suitable means of morphological prediction at present. Machine learning is particularly good at predicting the combined effect of complex factors, so this approach is attempted in this paper.

As can be seen from Fig. 21.a that the mathematical model based on the BP neural network was able to predict the probe deposition thickness well, with the 22,000 sets of predicted and original data all lying around the Y = X straight line, demonstrating good agreement between the model calculations and the original data. In order to further test the accuracy of the mathematical model, two additional sets of conditions were simulated, corresponding to the following simulation parameters. Validation case 1: particle concentration: 0.012 kg/m/s, air temperature: 1573 K, probe temperature: 453 K, flow velocity: 3 m/s, average particle size 31.5 μm. Validation case 2: particle concentration: 0.0533 kg/m/s, air temperature: 1623 K, probe temperature: 503 K, flow velocity: 2.8 m/s, average particle size 37.5 μm. Fig. 21.b shows the trend of the deposition thickness with the 1/4 probe circumference angle, and the machine learning results agree well with the simulation results. The errors for the two validation cases were 20.5% and 8.9%, respectively, and the errors between the mathematical model and the numerical calculations continued to decrease as the deposition thickness increased. At the same time, we acknowledge that the BP work in this paper may only be applicable to the ash properties simulated in this paper, and different deposition conditions can be borrowed but with reduced accuracy. However, considering the richness of the factors and raw data studied in this paper, the authors believed the prediction of the model may be in the right direction, and a certain degree of accuracy must be ensured. Scholars and engineers can modify the model to be more applicable to their own research conditions in the next period.

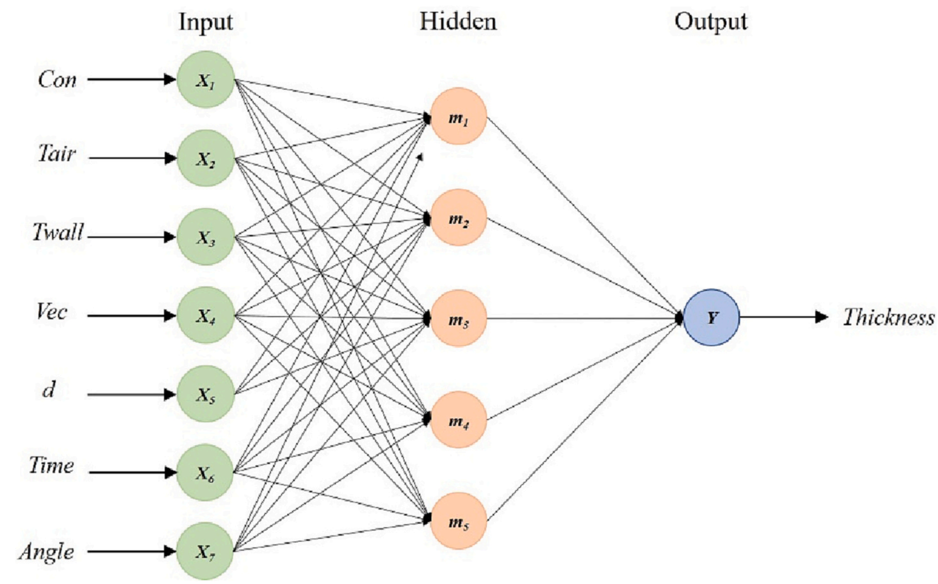

Fig. 20. BP neural network topology in present work.

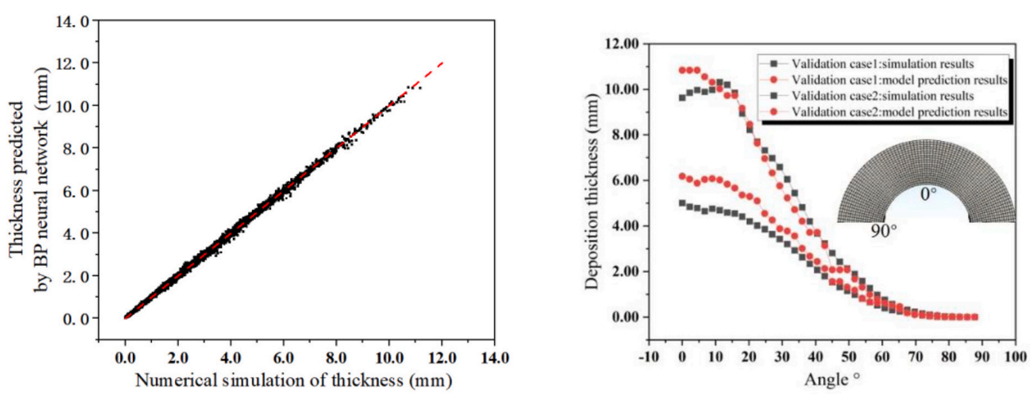

a Comparison of BP neural network learning results and original data

b Comparison of mathematical models and numerical simulations for validation cases

Fig. 21. A mathematical model of probe deposition thickness based on BP neural networks.

4. Conclusion

In the present work, an algorithm for ash particle deposition coupled with dynamic mesh, particle temperature model, erosion model, particle adhesion model and thermophoretic model is proposed which further improves the prediction accuracy of probe deposition thickness. The effects of flow rate, air temperature, probe temperature, mean particle size and concentration on probe deposition were calculated based on the proposed unified model. Results show that the proposed unified model has a prediction error of 7.66% for the probe deposition thickness. Impact and deposition efficiency always show opposite trends to factor changes. Concentration, particle size distribution and flow rate both affect the impact and deposition efficiency, but probe and air temperature only affect deposition efficiency. Deposition and impact efficiencies are dominated by particle temperature and size distribution, respectively. Impact efficiency of particles under different working conditions is distributed in the range of 50–65% and the deposition efficiency is distributed in the range of 5–25%, which get the efficiency of forming deposition of any ash particles in the boiler must be in the range of 2.5–16.25%. Different factors affect the deposition efficiency by influencing the particle temperature, the average particle temperature rises by 30 K with a double increase in flow rate. Also, a change of 10 to 30 K in particle temperature corresponds to a change of 100 K in air temperature. Mathematical models of PCA and BP neural networks were able to predict the maximum deposition thickness and probe deposition morphology with an error of 15% and 8.9%, which can provide a reference and base model for boiler operators and researchers. Moreover, scholars and engineers can modify the model to be more applicable based on their research conditions in the next period.

CRediT authorship contribution statement

Xiang Liu: Conceptualization, Writing – review & editing, Visualization, Supervision. **Xue Xue:** Methodology, Software, Validation. **Kelang Jin:** Formal analysis, Investigation, Data curation. **Lei Zhang:** Formal analysis. **Hao Zhou:** Project administration, Funding acquisition, Formal analysis, Investigation.

Declaration of Competing Interest

The authors declare that they have no known competing financial interests or personal relationships that could have appeared to influence the work reported in this paper.

Data availability

Data will be made available on request.

Acknowledgments

This work was supported by the National Science Fund for Distinguished Young Scholars (No.51825605), supported by the Fundamental Research Funds for the Central Universities (2022ZFJH004).

References

[1] Y. Jiang, G. Qiu, H. Wang, Modelling and experimental investigation of the full-loop gas–solid flow in a circulating fluidized bed with six cyclone separators, Chem. Eng. Sci. 109 (2014) 85–97.
[2] X. Yang, D. Ingham, L. Ma, H. Zhou, M. Pourkashanian, Understanding the ash deposition formation in Zhundong lignite combustion through dynamic CFD modelling analysis, Fuel 194 (2017) 533–543.
[3] S.V. Vassilev, K. Kitano, S. Takeda, T. Tsurue, Influence of mineral and chemical composition of coal ashes on their fusibility, Fuel Process. Technol. 45 (1) (1995) 27–51.
[4] H.P. Nielsen, L.L. Baxter, G. Sclippab, C. Morey, F.J. Frandsen, K. Dam-Johansen, Deposition of potassium salts on heat transfer surfaces in straw-fired boilers: a pilot-scale study, Fuel 79 (2) (2000) 131–139.
[5] S.S. Lokare, J.D. Dunaway, D. Moulton, D. Rogers, D.R. Tree, L.L. Baxter, Investigation of ash deposition rates for a suite of biomass fuels and fuel blends, Energy Fuel 20 (3) (2006) 1008–1014.
[6] J. Xu, D. Yu, B. Fan, X. Zeng, W. Lv, J. Chen, Characterization of ash particles from co-combustion with a Zhundong coal for understanding ash deposition behavior, Energy Fuel 28 (1) (2014) 678–684.
[7] C. Wieland, B. Kreutzkam, G. Balan, H. Spliethoff, Evaluation, comparison and validation of deposition criteria for numerical simulation of slagging, Appl. Energy 93 (2012) 184–192.
[8] P.M. Walsh, A.F. Sarofim, J.M. Beer, Fouling of convection heat exchangers by lignitic coal ash, Energy Fuel 6 (6) (1992) 709–715.
[9] M. Shimogori, T. Mine, N. Ohyatsu, N. Takarayama, Y. Matsumura, Effects of fine ash particles and alkali metals on ash deposition characteristics at the initial stage of ash deposition determined in 1.5MWth pilot plant tests, Fuel 97 (2012) 233–240.
[10] I. Naruse, D. Kamihashira, Miyauchi Y. Khairil, Y. Kato, T. Yamashita, et al., Fundamental ash deposition characteristics in pulverized coal reaction under high temperature conditions, Fuel 84 (4) (2005) 405–410.
[11] C. Liu, Z. Liu, T. Zhang, X. Huang, J. Guo, C. Zheng, Numerical investigation on development of initial ash deposition layer for a high-alkali coal, Energy Fuel 31 (3) (2017) 2596–2606.
[12] G. Li, S. Li, Q. Huang, Q. Yao, Fine particulate formation and ash deposition during pulverized coal combustion of high-sodium lignite in a down-fired furnace, Fuel 143 (2015) 430–437.
[13] L.L. Baxter, Ash Deposit Formation and Deposit Properties. A Comprehensive Summary of Research Conducted at Sandia's Combustion Research Facility, United States, 2000.
[14] R. Weber, N. Schaffel-Mancini, M. Mancini, T. Kupka, Fly ash deposition modelling: Requirements for accurate predictions of particle impaction on tubes using RANS-based computational fluid dynamics, Fuel 108 (2013) 586–596.
[15] R.P. Andres, Inelastic energy transfer in particle/surface collisions, Aerosol Sci. Technol. 23 (1) (1995) 40–50.
[16] R.A. Wessel, J. Righi, Generalized correlations for inertial impaction of particles on a circular cylinder, Aerosol Sci. Technol. 9 (1) (1988) 29–60.
[17] X. Yang, D. Ingham, L. Ma, A. Williams, M. Pourkashanian, Predicting ash deposition behaviour for co-combustion of palm kernel with coal based on CFD modelling of particle impaction and sticking, Fuel 165 (2016) 41–49.
[18] J.B. Young, Thermophoresis of a spherical particle: reassessment, clarification, and new analysis, Aerosol Sci. Technol. 45 (8) (2011) 927–948.
[19] H. Wiinikka, R. Gebart, The influence of fuel type on particle emissions in combustion of biomass pellets, Combust. Sci. Technol. 177 (4) (2005) 741–763.
[20] A.R. Mclennan, G.W. Bryant, B.R. Stanmore, T. Wall, Ash formation mechanisms during pf combustion in reducing conditions, Energy Fuel 14 (2000) 150–159.
[21] T.J. Taha, A.F. Stam, K. Stam, G. Brem, CFD modeling of ash deposition for co-combustion of MBM with coal in a tangentially fired utility boiler, Fuel Process. Technol. 114 (2013) 126–134.
[22] Z. Zhan, A.R. Fry, J.O.L. Wendt, Relationship between submicron ash aerosol characteristics and ash deposit compositions and formation rates during air- and oxy-coal combustion, Fuel 181 (2016) 1214–1223.
[23] W. Ai, J.M. Kuhlman, Simulation of coal ash particle deposition experiments, Energy Fuel 25 (2) (2011) 708–718.
[24] R. Weber, M. Mancini, N. Schaffel-Mancini, T. Kupka, On predicting the ash behaviour using computational fluid dynamics, Fuel Process. Technol. 105 (2013) 113–128.
[25] L. Mu, S. Wang, Z. Zhai, Y. Shang, C. Zhao, L. Zhao, et al., Unsteady CFD simulation on ash particle deposition and removal characteristics in tube banks: focusing on particle diameter, flow velocity, and temperature, J. Energy Inst. 93 (4) (2020) 1481–1494.
[26] H. Zhou, K. Zhang, Y. Li, J. Zhang, M. Zhou, Simulation of ash deposition in different furnace temperature with a 2D dynamic mesh model, J. Energy Inst. 92 (6) (2019) 1743–1756.
[27] M. Upadhyay, H.C. Park, J.G. Hwang, H.S. Choi, H.-N. Jang, Y.-C. Seo, Computational particle-fluid dynamics simulation of gas-solid flow in a circulating fluidized bed with air or O2/CO2 as fluidizing gas, Powder Technol. 318 (2017) 350–362.
[28] D.M. Snider, An incompressible three-dimensional multiphase particle-in-cell model for dense particle flows, J. Comput. Phys. 170 (2) (2001) 523–549.
[29] M.J. Andrews, P.J. O'Rourke, The multiphase particle-in-cell (MP-PIC) method for dense particulate flows, Int. J. Multiphase Flow 22 (2) (1996) 379–402.
[30] L. Talbot, R.K. Cheng, R.W. Schefer, D.R. Willis, Thermophoresis of particles in a heated boundary layer, J. Fluid Mech. 101 (4) (1980) 737–758.
[31] S. Black, J. Szuhánszki, A. Pranzitelli, L. Ma, P.J. Stanger, D.B. Ingham, et al., Effects of firing coal and biomass under oxy-fuel conditions in a power plant boiler using CFD modelling, Fuel 113 (2013) 780–786.
[32] R.I. Backreedy, J.M. Jones, L. Ma, M. Pourkashanian, A. Williams, A. Arenillas, et al., Prediction of unburned carbon and NOx in a tangentially fired power station using single coals and blends, Fuel 84 (17) (2005) 2196–2203.
[33] WE Ranz, WR Marshall, Evaporation from drops, part I, Chemical Eng. Progr. 48 (3) (1952) 141–146.
[34] H. Liu, M. Dong, W. Huang, J. Gao, K. Dai, J. Guo, et al., Lightweight conductive graphene/thermoplastic polyurethane foams with ultrahigh compressibility for piezoresistive sensing, J. Mater. Chem. C 5 (1) (2017) 73–83.
[35] H. Zhou, S. Hu, Numerical simulation of ash deposition behavior with a novel erosion model using dynamic mesh, Fuel 286 (2021), 119482.
[36] W. Ma, H. Zhou, J. Zhang, K. Zhang, D. Liu, C. Zhou, et al., Behavior of slagging deposits during coal and biomass co-combustion in a 300 kW down-fired furnace, Energy Fuel 32 (4) (2018) 4399–4409.
[37] A.M. Beckmann, M. Mancini, R. Weber, S. Seebold, M. Müller, Measurements and CFD modeling of a pulverized coal flame with emphasis on ash deposition, Fuel 167 (2016) 168–179.
[38] H. Zhou, B. Zhou, L. Li, H. Zhang, Investigation of the influence of the furnace temperature on slagging deposit characteristics using a digital image technique, Energy Fuel 28 (9) (2014) 5756–5765.
[39] Y. Liang, J. Li, X. Long, X. Lu, D. Zhang, A numerical simulation study of ash deposition in a circulating fluidized bed during Zhundong lignite combustion, Fuel 333 (2023), 126501.
[40] C. Xiaoxiao, Z. Yu, DriftScalarDyFoam: an OpenFOAM-based multistage solver for drifting snow and its distribution around buildings, Front. Earth Sci. (2022) 10.
[41] J. Li, M. Zhu, Z. Zhang, K. Zhang, G. Shen, D. Zhang, Characterisation of ash deposits on a probe at different temperatures during combustion of a Zhundong lignite in a drop tube furnace, Fuel Process. Technol. 144 (2016) 155–163.
[42] D.E. Rumelhart, G.E. Hinton, R.J. Williams, Learning representations by back-propagating errors, Nature 323 (1986) 533–536.